

Anti-dissipative strategies towards more efficient solar energy conversion

Agustina Cotic

INQUIMAE - CONICET

Simon Cerfontaine

Institut de la Matière Condensée et des Nanosciences <https://orcid.org/0000-0002-9865-762X>

Leonardo Slep

INQUIMAE - CONICET

Benjamin Elias

Université catholique de Louvain

Ludovic Troian-Gautier

Institut de la Matière Condensée et des Nanosciences

Alejandro Cadranel (✉ acadranel@qi.fcen.uba.ar)

INQUIMAE - CONICET <https://orcid.org/0000-0002-6597-4397>

Article

Keywords:

Posted Date: June 29th, 2022

DOI: <https://doi.org/10.21203/rs.3.rs-1760783/v1>

License:   This work is licensed under a Creative Commons Attribution 4.0 International License.

[Read Full License](#)

Anti-dissipative strategies towards more efficient solar energy conversion

Agustina Cotic,^{a,b} Simon Cerfontaine,^c Leonardo Slep,^{a,b} Benjamin Elias,^c Ludovic Troian-Gautier,^c * and Alejandro Cadranel^{a,b,d,e} *

a Universidad de Buenos Aires, Facultad de Ciencias Exactas y Naturales, Departamento de Química Inorgánica, Analítica y Química Física, Pabellón 2, Ciudad Universitaria, C1428EHA, Buenos Aires, Argentina.

b CONICET – Universidad de Buenos Aires, Instituto de Química-Física de Materiales, Medio Ambiente y Energía (INQUIMAE), Pabellón 2, Ciudad Universitaria, C1428EHA, Buenos Aires, Argentina.

c Université catholique de Louvain (UCLouvain), Institut de la Matière Condensée et des Nanosciences (IMCN), Molecular Chemistry, Materials and Catalysis (MOST), Place Louis Pasteur 1, bte L4.01.02, 1348 Louvain-la-Neuve, Belgium

d Friedrich-Alexander-Universität Erlangen-Nürnberg (FAU), Physical Chemistry I, Egerlandstr. 3, 91058, Erlangen, Germany.

e Friedrich-Alexander-Universität Erlangen-Nürnberg (FAU), Interdisciplinary Center for Molecular Materials, Egerlandstr. 3, 91058, Erlangen, Germany.

*Correspondence to: Ludovic.Troian@uclouvain.be, acadranel@qi.fcen.uba.ar

ABSTRACT: In natural and artificial photosynthesis, light absorption and catalysis are separate processes linked together by exergonic electron transfer. This leads to free energy losses between the initial excited state, formed after light absorption, and the catalytic center formed after the electron transfer cascade. Additional deleterious processes, such as internal conversion and vibrational relaxation, also dissipate as much as 20-30 % of the absorbed photon energy.

Minimization of these energy losses, a holy-grail in solar energy conversion and solar fuels production, is a challenging task, because excited states are usually strongly coupled which results in negligible kinetic barriers and very fast dissipation. Here we show that topological control of oligomeric $\{\text{Ru}(\text{bpy})_3\}$ chromophores resulted in small excited-state electronic couplings, leading to activation barriers for internal conversion of around 2000 cm^{-1} and effectively slowing down dissipation. Two types of excited states are populated upon visible light excitation, *i.e.* a bridging-ligand centered metal-to-ligand charge transfer (MLCT_{Lm}), and a 2,2'-bipyridine-centered MLCT (MLCT_{bpy}), which lies $800\text{-}1400\text{ cm}^{-1}$ higher in energy. As a proof-of-concept, bimolecular electron transfer with tri-tolylamine as electron donor was performed, which mimics catalyst activation by sacrificial electron donors in typical photocatalytic schemes. Both excited states were efficiently quenched by tri-tolylamine and produced the corresponding $\text{bpy}^{\bullet-}$ and $\text{Lm}^{\bullet-}$ centered reduced complexes, as confirmed by transient absorption spectroscopy. This efficiently generated two distinct reduced photosensitizers with different reducing abilities, *i.e.* -0.93 V and -0.79 V vs NHE for $\text{bpy}^{\bullet-}$ and $\text{Lm}^{\bullet-}$, respectively. Hence, this novel strategy not only allows to trap higher energy excited states, before internal conversion and vibrational relaxation set in, saving between 110 and 170 meV and but also leads *in fine* to 140 meV more potent reductant for energy conversion schemes and solar fuels production. These results lay the first stone for anti-dissipative energy conversion schemes which, in bimolecular electron transfer reactions, harnesses the excess energy saved by controlling dissipative conversion pathways.

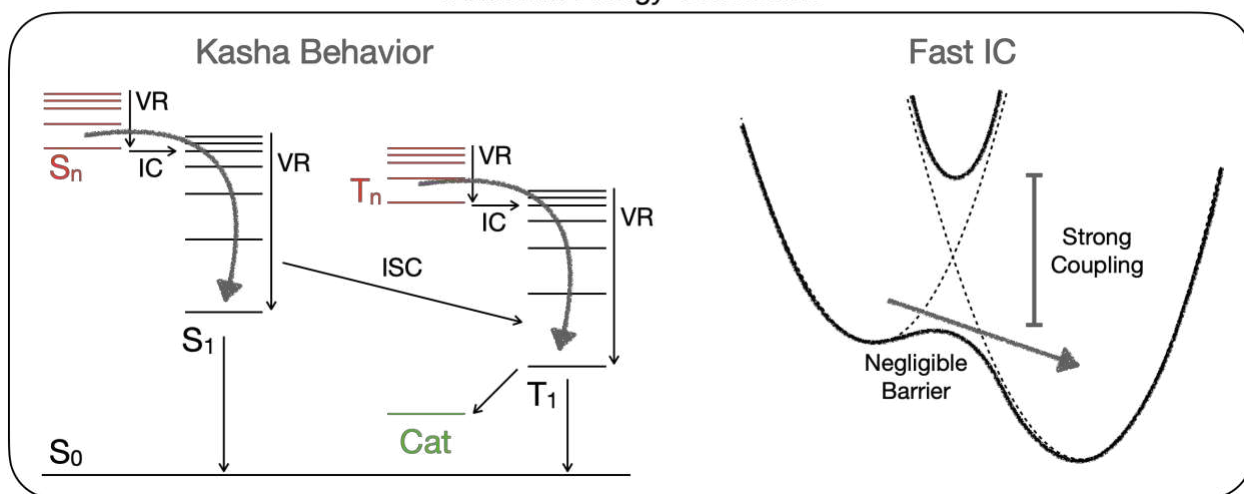
Introduction

In natural photosynthesis, early time-scale dynamics, that include vibrational relaxation (VR) and internal conversion (IC) in molecular chromophores, are exergonic, and can dissipate around 20-30 % of the absorbed photon energy that could otherwise be transformed into useful

chemical potential.¹ Artificial molecular approaches to solar energy conversion suffer from analogous energy losses. It is therefore of paramount importance to tame these dissipative pathways for efficient and optimal solar energy conversion schemes. To this end, dissipative processes in singlet fission² or in hot carrier solar cells³ were previously explored. Ultimately, photosynthesis was re-wired to promote electron extraction directly from photoexcited photosystems, avoiding the electron transfer reaction chain which dissipates energy.⁴

In the vast majority of molecular chromophores, according to Kasha's rule, VR and IC are usually fast and take place before any bimolecular or long range reactivity (Figure 1, top).⁵ IC involves an isoenergetic transformation between excited states of the same multiplicity, so it is not dissipative *per se*. However, IC usually generates a vibrationally excited molecular entity, which dissipates energy to the medium via VR to reach the lowest excited state. The key to trap high-energy excited states is to delay IC/VR-mediated dissipation pathways, so that energy demanding bimolecular chemistry that leverages the excess energy, such as electron transfer to create a catalytic reaction centre, can be performed. Ideally, the activated catalytic site inherits the excess driving force, which translates into enhanced oxidative / reductive potentials, and persists long enough to react with specific substrates. This scheme of anti-dissipative energy conversion could lead to significant improvements in energy conversion devices, photoredox catalysis and solar fuels production.

Traditional Energy Conversion



Anti-Dissipative Energy Conversion

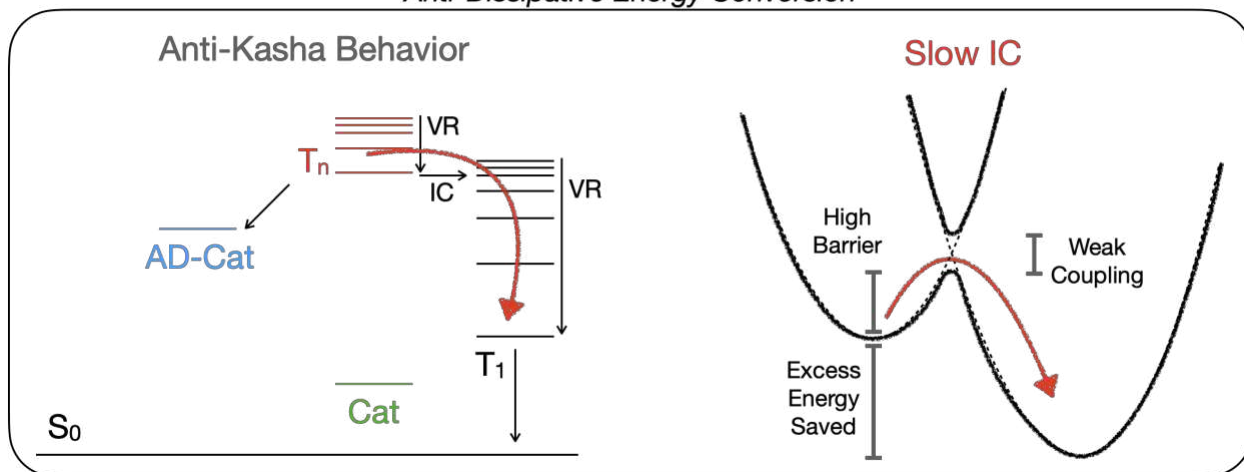


Figure 1: Top: Jablonski-Perrin diagram and schematic representation of Kasha scenarios, with strong electronic coupling between excited states and fast IC, in traditional energy conversion. Bottom: The anti-dissipative energy conversion approach requires anti-Kasha scenarios, with weak electronic coupling between the excited states and slow IC, that allows to activate high-energy catalysts. (IC: internal conversion, VR: vibrational relaxation, ISC: intersystem crossing, AD-Cat: anti-dissipative catalyst, Cat: traditional catalyst).

Kasha's rule is substantiated in strong electronic coupling between the different excited states, which results in negligible barriers for IC/VR dissipative pathways (**Figure 1**, top). Therefore, poor excited-state electronic coupling scenarios, where high kinetic barriers mediate IC/VR (**Figure 1**, bottom), must be explored to realize anti-Kasha photochemistry and anti-

dissipative energy conversion. Observations involving a variety of intramolecular donor/bridge/acceptor processes, ranging from singlet fission to ground- and excited-state intervalence charge transfers,⁶⁻¹⁵ suggest that the topology of the bridge can be exploited to modulate excited-state electronic coupling.^{16,17} Prototypical polynuclear ruthenium polypyridines^{18,19} provide an ideal platform for these studies because their excited states have clear spectroscopic handles, with well-defined long-lived metal-to-ligand charge transfer (MLCT) transitions and they are widely used in energy conversion schemes and photoredox catalysis.²⁰ This attracted our attention to D_p and D_m (**Figure 2**), which are $\{\text{Ru}(\text{bpy})_3\}$ dimers with outstanding properties in terms of light absorption, photostability^{21,22} and photoredox catalytic activity.²³ Their structures differ in the topology of the bridging ligands L_p and L_m , where the 2,2'-bipyridine fragments are either connected via the 4 (*para*) or 5 (*meta*) positions, respectively.

Recently, it was shown that D_p behaves as a typical Kasha chromophore.¹⁵ The excited state behavior is dominated by lowest triplet state, which is an emissive Metal-to-Ligand Charge Transfer $^3\text{MLCT}(L_p)$ state. It includes a bridging ligand radical anion according to spectroelectrochemistry.¹⁵ Only very minor differential spectral changes were observed from the pico- to the microsecond timescale by transient absorption spectroscopy (TAS), highlighting that the changes of excited-state electronic configuration associated to IC occurred on the sub-picosecond timescale. Upon excitation and intersystem crossing, vibrationally hot $^3\text{MLCT}(L_p)$ relaxed to the thermally-equilibrated $^3\text{MLCT}(L_p)$ in less than 10 ps, typical for vibrational relaxation processes in $[\text{Ru}(\text{bpy})_3]^{2+}$ and other ruthenium polypyridine chromophores.²⁴⁻²⁹ Electronic coupling between the different excited states is strong and favored an efficient IC without any significant kinetic barriers (**Figure 1**, top), leading to the population of the lowest triplet state in a few picoseconds, like in $[\text{Ru}(\text{bpy})_3]^{2+}$. We hypothesized that the topology of the

bridge in D_m could lead to an anti-Kasha scenario, fulfilling the requirements for an anti-dissipative photosensitizer / photocatalyst. Thus, we sought to explore the IC/VR dissipative pathways of D_m , by means of TAS in the femtosecond (fsTAS) and nanosecond (nsTAS) ranges. We also extended the analysis to a series of trinuclear ruthenium(II) chromophores (**Figure 2**) with *para* substitution topology (T_{pm} , T_{mp}) and *meta* substitution topology (T_{mm}).³⁰ To mimic catalyst activation, proof-of-concept electron transfer reactions from a tri-tolylamine (TTA) electron donor were investigated in an anti-dissipative energy conversion scheme model.

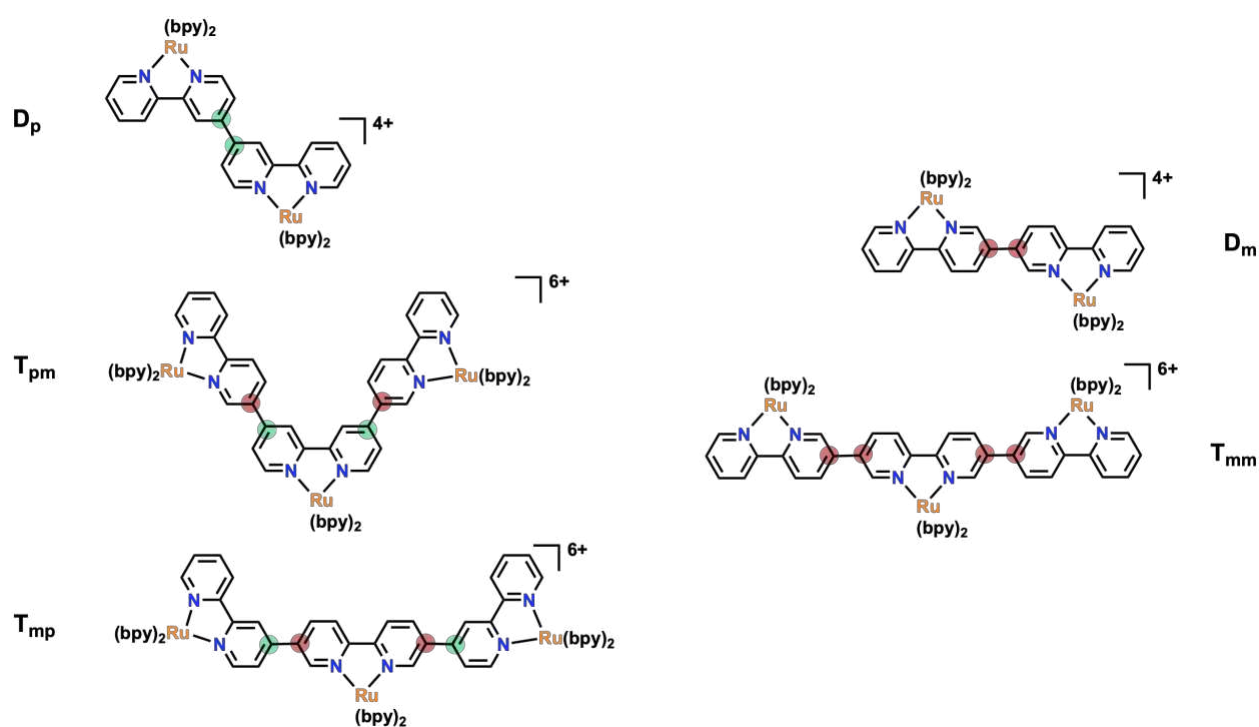


Figure 2. Structures of the polynuclear ruthenium (II) bipyridines photosensitizers studied in this work. Green and red carbon atoms denote *para* and *meta* connections in the bridging ligands, respectively. They are grouped according to their photophysical behavior (see text). The polynuclear complexes studied herein are a mixture of diastereoisomers due to the presence of Λ and Δ enantiomers on the Ru(II) centers. Previous reports on resolved polynuclear complexes suggest that the presence of stereoisomers is unlikely to affect the photophysical properties and that electronic factors are the main contributors of excited-state properties.^{31–33}

Results and Discussion

We started exploring the early nanosecond timescales on D_m using nsTAS with 460 nm (21200 cm^{-1}) excitation (delay times $> 1\text{ ns}$, 1 ns time resolution). In contrast to D_p , the excited state decay of D_m is best described using two exponential decays (**Figures 3** and **S1**). A close inspection of the kinetic trace at 20500 cm^{-1} (488 nm) revealed a rise in the first 30 ns, before the signal decayed to zero indicating ground-state recovery. This implied that, besides the longest-lived ${}^3\text{MLCT}(L_m)$ state, an additional excited state participated to the decay cascade. A target analysis strategy was employed to obtain lifetimes and species associated differential spectra for both states. This method afforded excited-state lifetimes of 16 and 515 ns, together with the differential spectra shown in **Figure 3**. The longest lifetime and its associated differential spectrum matched those obtained for the emissive ${}^3\text{MLCT}(L_m)$, which also include bridging ligand radical anions according to spectroelectrochemistry (**Figure S2** and details in the SI).^{15,21} This excited state also featured a photoinduced absorption at 8400 cm^{-1} (1190 nm) assigned to a photoinduced intervalence charge transfer (PIIVCT) involving the two Ru ions, originating in a $\{\text{Ru}^{\text{III}-\delta}(\text{L}_m^{\bullet-})\text{Ru}^{\text{II}+\delta}\}$ electronic configuration for ${}^3\text{MLCT}(L_m)$. Similar PIIVCT were also observed for ${}^3\text{MLCT}(L_p)$.¹⁵ DFT and TD-DFT calculations of the lowest triplet state of D_m (**Figures S3-S4**, **Tables S1-S2**, and details in the SI) were consistent with our experimental interpretation.

The differential spectrum of the shorter-lived species observed in nsTAS of D_m (**Figure 3**, **Figure S5** and details in the SI) closely resembled the one of $[\text{Ru}(\text{bpy})_3]^{2+}$ and was therefore assigned to a ${}^3\text{MLCT}(\text{bpy})$ state, where the excited electron is located on an ancillary bpy ligand. The ${}^3\text{MLCT}(\text{bpy})$ shows weak signals in the NIR, consistent with poor metal-metal electronic coupling and a $\{(\text{bpy}^{\bullet-})\text{Ru}^{\text{III}}(\text{L}_m)\text{Ru}^{\text{II}}\}$ electronic configuration. Thus, an anti-Kasha picture is observed for D_m , with coexisting ${}^3\text{MLCT}(L_m)$ and ${}^3\text{MLCT}(\text{bpy})$ excited-state populations (Eq 1

and 1') that persist until 1500 and 50 nanoseconds, respectively, indicative of a slowed and activated IC between them (Eq 2). As observed by fsTAS, an early population distribution between $^3\text{MLCT}(\text{L}_m)$ and $^3\text{MLCT}(\text{bpy})$ occurred, concomitant with vibrational relaxation (**Figures S6-S7**, details in the SI). These observations imply high kinetic barriers and poor electronic coupling between $^3\text{MLCT}(\text{L}_m)$ and $^3\text{MLCT}(\text{bpy})$ (**Figure 1**).

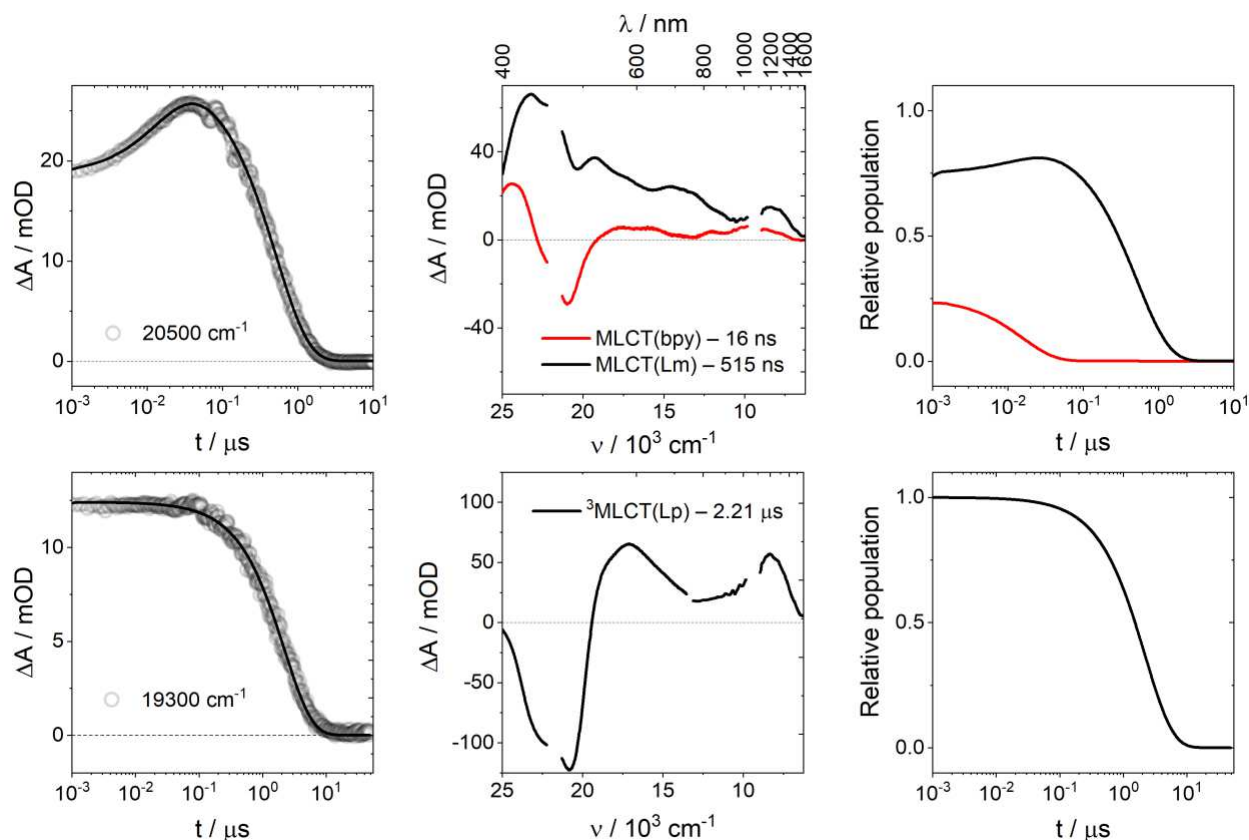
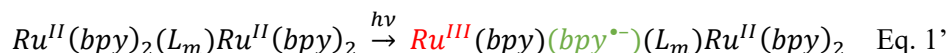
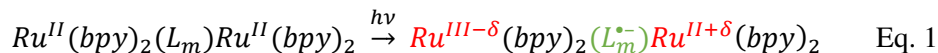


Figure 3. nsTAS with 460 nm excitation of D_m (top) and D_p (bottom) in argon-purged acetonitrile at room temperature. Differential absorption kinetic traces at 20500 cm⁻¹ (top left) and 19300 cm⁻¹ (bottom left), Species associated differential spectra of $^3\text{MLCT}(\text{bpy})$ (red spectrum) and $^3\text{MLCT}(\text{L}_m)$ (black spectrum) (top center), and

$^3\text{MLCT}(\text{L}_p)$ (bottom center), and time evolution of the relative populations of $^3\text{MLCT}(\text{bpy})$ (red curve) and $^3\text{MLCT}(\text{L}_m)$ (black curve) (top right), and $^3\text{MLCT}(\text{L}_p)$ (bottom right).

Table 1. Excited-state properties and thermodynamic parameters for the series of binuclear and trinuclear photosensitizers studied herein.

Excited State	D_m		T_{mm}		D_p	T_{mp}	T_{pm}
	$^3\text{MLCT}(\text{L}_m)$	$^3\text{MLCT}(\text{bpy})$	$^3\text{MLCT}(\text{L}_{mm})$	$^3\text{MLCT}(\text{bpy})$	$^3\text{MLCT}(\text{L}_p)$	$^3\text{MLCT}(\text{L}_{mp})$	$^3\text{MLCT}(\text{L}_{pm})$
τ (ns)	515	16	312	9	2210	149	559
E_0 (cm^{-1})	16400	17200	15800	17200	15900	15100	15800
E_{a-IC} (cm^{-1})		2060		1940	n.d.	n.d.	n.d.
A_{IC} (s^{-1})		5×10^{11}		4×10^{11}	n.d.	n.d.	n.d.
k_{IC1} (s^{-1}) ^a		2.3×10^7		3.3×10^7	10^{11} - 10^{12}	10^{11} - 10^{12}	10^{11} - 10^{12}
ΔG_{IC} (cm^{-1})		800		1400	1300	2100	1400

^a At 298 K. n.d.: non determined

The $^3\text{MLCT}(\text{bpy}) \rightarrow ^3\text{MLCT}(\text{L}_m)$ population transfer was estimated as 800 cm^{-1} downhill, since the triplet energy E_0 for $^3\text{MLCT}(\text{bpy})$ is expected to be close to the one of $[\text{Ru}(\text{bpy})_3]^{2+}$ (17200 cm^{-1}), while E_0 for $^3\text{MLCT}(\text{L}_m)$ is 16400 cm^{-1} .²¹ Unequivocal evidence of $^3\text{MLCT}(\text{bpy}) \rightarrow ^3\text{MLCT}(\text{L}_m)$ internal conversion activity was collected from temperature dependent nsTAS, where $^3\text{MLCT}(\text{bpy})$ lifetimes were monitored from 290 to 350 K for D_m in butyronitrile (**Figure 4** and details in the SI). Decay of the $^3\text{MLCT}(\text{bpy})$ states includes contributions from direct radiative (k_{dr}) and non-radiative (k_{dnr}) transitions to the ground state, and, in principle, two activated processes that could potentially take place, namely $^3\text{MLCT}(\text{bpy}) \rightarrow ^3\text{MLCT}(\text{L}_m)$ (k_{IC1}) and $^3\text{MLCT}(\text{bpy}) \rightarrow ^3\text{MC}$ (k_{IC2}) internal conversions. This is represented in equation (2), where each of the activated terms involves a pre-exponential factor (A) and an activation energy (E_a).

$$\frac{1}{\tau(T)} = k_{dr} + k_{dnr} + k_{IC1}(T) + k_{IC2}(T) = k_{dr} + k_{dnr} + A_1 e^{\frac{-E_{a1}}{RT}} + A_2 e^{\frac{-E_{a2}}{RT}} \quad (2)$$

$$\frac{1}{\tau(T)} = k_{dr} + k_{dnr} + A_1 e^{\frac{-E_{a1}}{RT}} \quad (3)$$

For $^3\text{MLCT}(\text{bpy})$ in D_m , only one activated term was sufficient to accurately account for the experimental observations (**Figure 4**) in the entire temperature range investigated herein. This enabled a modified Arrhenius analysis using equation (3) that yielded an activation energy of 2060 cm^{-1} , and a pre-exponential factor of $5 \times 10^{11} \text{ s}^{-1}$. In this analysis, the non-exponential term $k_{\text{dr}} + k_{\text{dnr}}$ was fixed to its value for $^3\text{MLCT}(\text{bpy})$ in $[\text{Ru}(\text{bpy})_3]^{2+}$, $4.1 \times 10^5 \text{ s}^{-1}$ (see the SI for details).²¹ $k_{\text{dr}} + k_{\text{dnr}}$ values between $1 \times 10^4 \text{ s}^{-1}$ and $1 \times 10^6 \text{ s}^{-1}$ afforded identical results, while $1 \times 10^7 \text{ s}^{-1}$ led to noticeable deviations from the experimental data points. A schematic Jablonski diagram describing the excited decay cascade for D_m is depicted in **Figure 5** and a discussion about the different contributions to the decay of $\text{MLCT}(\text{bpy})$ in D_m is presented in the supporting information (**Figure S8**). Most importantly, the IC rate constant k_{IC1} observed for D_m at room temperature, $2.2 \times 10^7 \text{ s}^{-1}$, is at least four orders of magnitude smaller than those for VR and IC in usual chromophores like D_p and $[\text{Ru}(\text{bpy})_3]^{2+}$, where values of 10^{11} - 10^{12} s^{-1} are usually obtained.^{26,27,29,34,35}

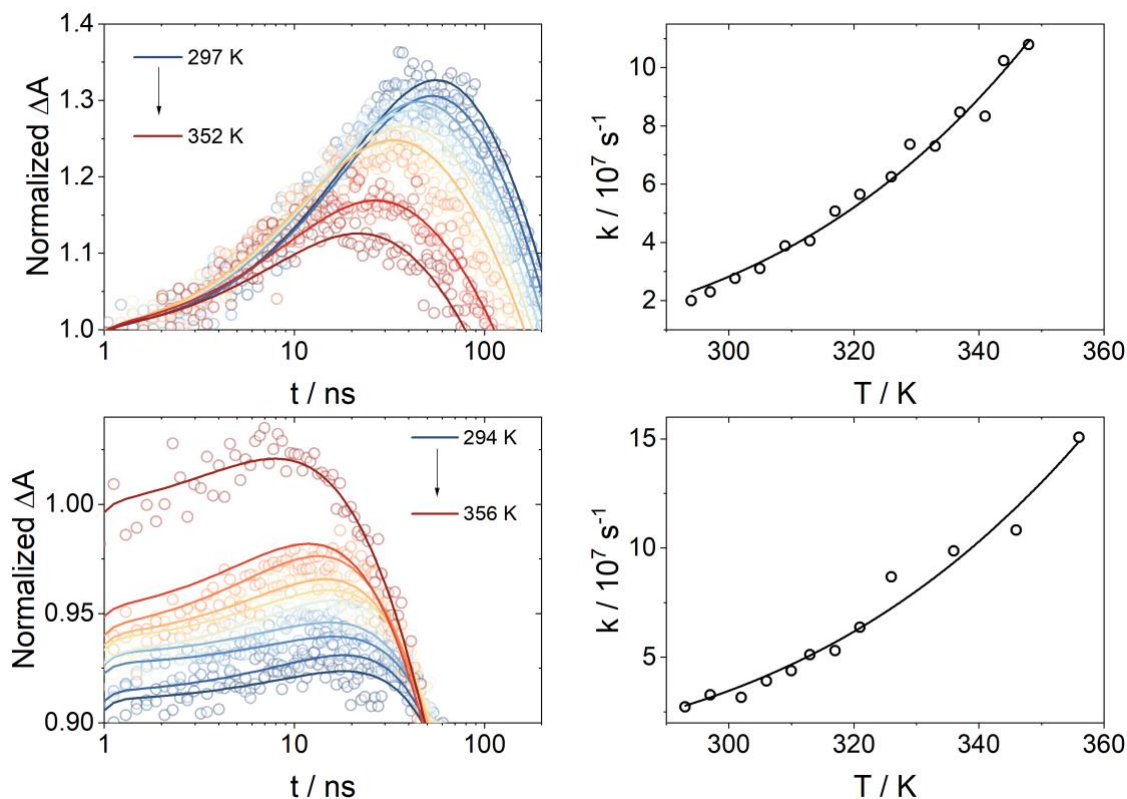


Figure 4. Left: Experimental kinetic traces (dots) and best fits (lines) at 20500 cm^{-1} (488 nm) for D_m (top) and at 18550 cm^{-1} (539 nm) for T_{mm} (bottom). Right: Decay constants (dots) of the $^3\text{MLCT}(\text{bpy})$ states derived from nsTAS of D_m (top) and T_{mm} (bottom) in butyronitrile, and best fits according to a modified Arrhenius analysis (lines).

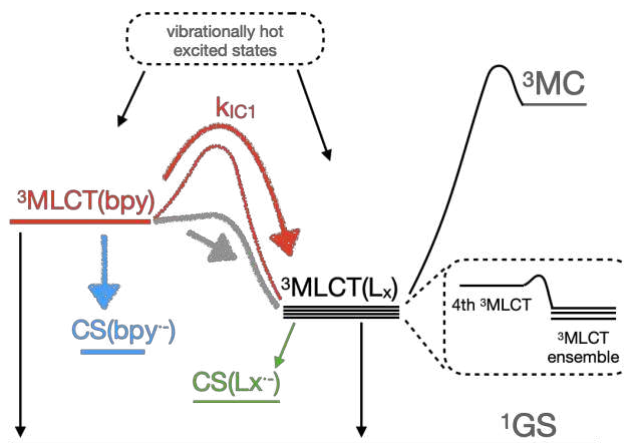


Figure 5. Schematic Jablonski-Perrin diagrams showing the excited state cascade for D_p , T_{mp} and T_{pm} , which include a fast IC (grey arrow) and electron transfer in the presence of an electron donor (green arrow), generating a charge separated (CS) product $\text{CS}(\text{L}_x^-)$, where L_x is either L_m or L_{mm} . For D_m and T_{mm} , a slow IC (red arrow) allows the interception of high energy excited states via electron transfer (blue arrow) in the presence of an electron donor, generating a high-energy charge separated product, $\text{CS}(\text{bpy}^-)$.

The results presented herein indicate that an all-*meta* substitution pattern, like in D_m and T_{mm} , is key to slow down IC. Indeed, nsTAS at room temperature of the all *meta*-connected trinuclear complex T_{mm} (**Figure 2**) afforded results analogous to those for D_m , with lifetimes of 9 and 312 ns for ${}^3\text{MLCT}(\text{bpy})$ and ${}^3\text{MLCT}(\text{L}_{mm})$, respectively (**Figure S9**). For T_{mm} , the modified Arrhenius analysis yielded $E_a = 1940 \text{ cm}^{-1}$ and $A = 4 \times 10^{11} \text{ s}^{-1}$ (**Figure 4**), and $k_{IC1} = 3.2 \times 10^7 \text{ s}^{-1}$ at room temperature, all very similar to those obtained for D_m . In contrast, introduction of *para*-connections vicinal to *meta*-connections, as in T_{mp} and T_{pm} (**Figure 1**), is sufficient to reinstate electronic coupling and generate a fast IC between ${}^3\text{MLCT}(\text{bpy})$ and ${}^3\text{MLCT}(\text{L}_{mp}/\text{L}_{pm})$, respectively. In fact, nsTAS at room temperature of both T_{mp} and T_{pm} can be adequately described, like that of D_p , using only one exponential decay of 149 and 559 ns, respectively (**Figures S10-S11**). E_0 of the emissive states is 15800 cm^{-1} for T_{mm} , and 15900, 15100 and 15800 cm^{-1} , for D_p , T_{mp} and T_{pm} , respectively.³⁰ This afforded driving forces for the downhill IC processes of 1400 cm^{-1} for T_{mm} , and 1300, 2100 and 1400 cm^{-1} , for D_p , T_{mp} and T_{pm} , respectively. In comparison with the 800 cm^{-1} estimated above for D_m , it appears that no clear trend is discernible and that, to the extent of the temperature range explored herein, the IC process is not modulated by the driving force.

In fact, it appears that the topology of the bridge is the main contributor to control the dissipative IC pathways in the chromophores studied here. Since interchromophore distance variations are minimal along the series explored, through-space interactions between the excited states involved in the IC process probably remain similar. However, one of the main consequences of changing the topology of the bridge is related to the dihedral angle between the different $\{\text{Ru}(\text{bpy})_3\}$ fragments within an oligonuclear chromophore, which can modulate through-bond interchromophore interactions. In the ground state, the calculated DFT structures of D_p ¹⁵ and D_m

($\Lambda\Lambda$ diastereoisomer) (**Figures S12-S13, Tables S4-S6**) afford identical dihedral angles of 30° within the bridging ligand, both strongly deviated from planarity. $^3\text{MLCT}(\text{bpy})$ states in D_p (which are not observed experimentally but exist) and D_m are also expected to have similar dihedral angles of 30° , because the bridging ligands are present in their non-reduced forms like in the ground state. However, the calculated DFT structures of $^3\text{MLCT}(\text{L}_p)$ and $^3\text{MLCT}(\text{L}_m)$, which include $\text{L}_p^{\bullet-}$ and $\text{L}_m^{\bullet-}$ radical anions, afford dihedral angles of 4 and 16° , respectively (**Table S5**).¹⁵ Hence, while $\text{L}_p^{\bullet-}$ is almost perfectly planar, $\text{L}_m^{\bullet-}$ significantly deviates from planarity. It is therefore likely that the bridging ligand dihedral angles within the $^3\text{MLCT}(\text{L}_m/\text{L}_{mm})$ excited states of D_m and T_{mm} , respectively, lead to a poor overlap of the electronic wave functions of the excited states involved. In this picture, the hindrance of through-bond interactions is the physical origin of the IC barrier in the all-*meta*-connected chromophores. In contrast, when a *para*-substitution is present, the bridging ligand radical anions approach planarity, promoting an efficient overlap of the electronic wave functions of the excited states involved, reinstating through-bond interactions and a fast IC.

With this clear excited state description, we noticed that the higher energy excited state $^3\text{MLCT}(\text{bpy})$ of D_m and T_{mm} was sufficiently long-lived to perform bimolecular electron transfer,³⁶ and could hence be intercepted before IC/VR for anti-dissipative energy conversion. These higher energy-state could save between 800 cm^{-1} (100 meV) and 1400 cm^{-1} (170 meV) for D_m and T_{mm} , respectively. As a proof-of-concept for anti-dissipative catalyst activation, we investigated bimolecular electron transfer using tri-tolylamine (TTA) as an electron donor and D_m as an electron acceptor by means of nsTAS. This reaction mimics catalyst activation by (sacrificial) electron donors in reductive photocatalysis like CO_2 reduction or other photoredox schemes.^{23,37} The formation of oxidized tri-tolylamine ($\text{TTA}^{+\bullet}$) was clearly evident in nsTAS (**Figures 6a, S14-S17**) through the large absorption changes observed in the $15000\text{-}20000\text{ cm}^{-1}$ (500-800 nm) range, with

a maximum at 14900 cm^{-1} (670 nm).³⁶ To provide insights into the electron transfer mechanism, different amounts of TTA were added to solutions of D_m , and a target analysis of the nsTAS results was applied (**Figures 6** and **S13-S15**). The resulting ${}^3\text{MLCT}(L_m)$ and ${}^3\text{MLCT}(\text{bpy})$ decay constants were found to increase upon the addition of TTA (**Figure 6e-f** and **Table S7**) which were analyzed according to equation (4).

$$k_{obs} = k_0 + k_{eT}[TTA] \quad (4)$$

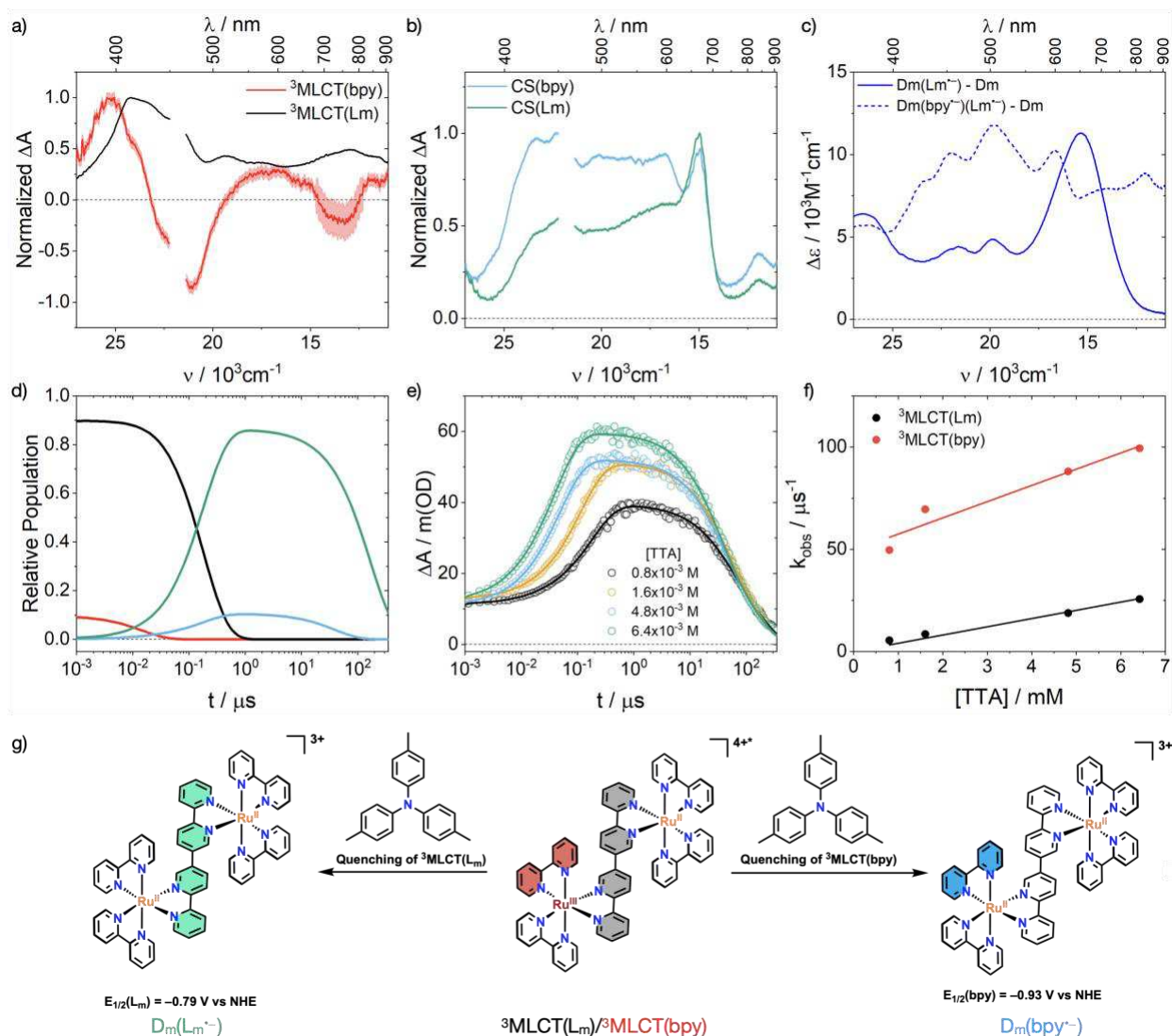
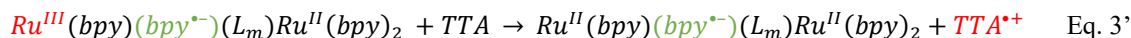


Figure 6. nsTAS of D_m (3.8 mM) with 0.8 mM TTA in acetonitrile at room temperature. a) Species associated differential spectra of ${}^3\text{MLCT}(\text{bpy})$ (red), ${}^3\text{MLCT}(L_m)$ (black). b) Species associated differential spectra of $\text{CS}(\text{bpy}^{\bullet-})$ (cyan), $\text{CS}(L_m^{\bullet-})$ (green). c) Differential spectra obtained upon one-electron (solid blue line) and two-electron (dashed blue line) processes. d) Relative populations of ${}^3\text{MLCT}(L_m)$ (black) and ${}^3\text{MLCT}(\text{bpy})$ (red) over time. e) Decay of ${}^3\text{MLCT}(L_m)$ (black) and ${}^3\text{MLCT}(\text{bpy})$ (red) over time for different [TTA] concentrations. f) Observed decay constant k_{obs} vs [TTA] for ${}^3\text{MLCT}(L_m)$ (black) and ${}^3\text{MLCT}(\text{bpy})$ (red). g) Chemical structures showing the quenching of ${}^3\text{MLCT}(L_m)$ (3+) and ${}^3\text{MLCT}(\text{bpy})$ (4+) by TTA to form $D_m(L_m^{\bullet-})$ and $D_m(\text{bpy}^{\bullet-})$ respectively. Redox potentials: $E_{1/2}(L_m) = -0.79 \text{ V vs NHE}$ and $E_{1/2}(\text{bpy}) = -0.93 \text{ V vs NHE}$.

(dashed blue line) reduction of D_m in acetonitrile. d) Relative population of the different ³MLCT(bpy) (black), ³MLCT(L_m) (red), CS(bpy^{•-}) (cyan), CS(L_m^{•-}) (green). e) Kinetic traces at 670 nm (dots) and fits (lines) derived from nsTAS of D_m solutions in argon-purged acetonitrile, with different concentrations of TTA. f) Observed decay constant of ³MLCT(L_m) (black dots) and ³MLCT(bpy) (red dots) derived from nsTAS and linear fits, which afforded bimolecular quenching rate constants (*k_q*) of 4.0 x 10⁹ M⁻¹s⁻¹ and 7.9 x 10⁹ M⁻¹s⁻¹ for ³MLCT(L_m) and ³MLCT(bpy), respectively. g) Strategies for quenching higher energy states using tri-tolylamine as electron donor. The different excited state, i.e. ³MLCT(bpy) and ³MLCT(L_m) are represented by the red and black coloring, respectively. Excited-state electron transfer with tri-tolylamine (TTA) shows the formation of CS(bpy^{•-}) (right, blue) and CS(L_m^{•-}, green) and the corresponding TTA^{•+} (not shown)

Linear fits afforded bimolecular quenching rate constants (*k_q*) of 4.0 x 10⁹ M⁻¹s⁻¹ and 7.9 x 10⁹ M⁻¹s⁻¹ for ³MLCT(L_m) and ³MLCT(bpy), respectively (**Figure 6f**). These *k_q* are in agreement with diffusion limited processes for catalyst activation. The nature of the activated catalyst models formed in the bimolecular electron transfer reactions, *i.e.* the charge separated (CS) states, was revealed by nsTAS. Besides quenching of ³MLCT(L_m) and ³MLCT(bpy) in the sub-μs timescale, a biexponential decay is detected in the μs timescale. The species associated differential spectra obtained for the two long-lived CS species (**Figure 6b**) both include a sharp maximum at 14900 cm⁻¹ (670 nm) ascribed to TTA^{•+}. However, enhanced absorptions above 16000 cm⁻¹ and below 14000 cm⁻¹ are observed for one of the CS species. Very similar features are obtained in reductive spectroelectrochemistry of D_m, which reveals enhanced absorptions above 16400 cm⁻¹ (625 nm) and below 14400 cm⁻¹ (694 nm) for bpy^{•-} in comparison with L_m^{•-} (Figure 6c). This demonstrates that both radical anions are produced in the reaction with TTA. According to our models, electron transfer from TTA to D_m undergoes two main pathways (**Figure 6g**):



While reaction 3 generated a trivial $D_m(L_m^{\bullet-})$ radical anion, this is, with the additional electron located on the LUMO, reaction 3' produced a high energy, non-conventional LUMO+1 anion $D_m(bpy^{\bullet-})$. This result highlights the unique usefulness of light conversion, since generation of LUMO+1 anions is impossible by solely electrochemical methods. Reduction potentials of -0.93 V and -0.79 V vs NHE for $bpy^{\bullet-}$ and $L_m^{\bullet-}$, respectively, show that the 110 meV saved by blocking excited-state dissipation are translated into a 140 meV more potent reductive photocatalyst. Charge recombination between TTA^{*+} and $D_m(bpy^{\bullet-})$ is around five times faster than that one between TTA^{*+} and $D_m(L_m^{\bullet-})$ (**Table S6**), consistent with a higher driving force for back electron transfer from $bpy^{\bullet-}$. Notably, this high energy radical anion lives for around 30 μ s.

Conclusion

Topological control of dissipative IC/VR processes was demonstrated in polynuclear $\{Ru(bpy)_3\}$ photosensitizers. Activation barriers for IC of around 2000 cm^{-1} allowed to trap high-energy excited states $800\text{-}1400\text{ cm}^{-1}$ (100-170 meV) over the lowest excited state. This excess energy was capitalized performing proof-of-concept bimolecular electron transfer reactions with a tri-tolylamine electron donor, which mimics catalyst activation by a sacrificial electron donor. This reaction produced high-energy reducing agents, 140 meV more powerful than the one generated from the lowest excited state. This amount of spared energy is significant for solar energy conversion schemes and solar fuels production and offers a novel economic pathway to prevent energy losses in anti-dissipative energy conversion schemes.

References

1. Gust, D., Kramer, D., Moore, A., Moore, T. A. & Vermaas, W. Engineered and artificial photosynthesis: Human ingenuity enters the game. *MRS Bull.* **33**, 383–387 (2008).
2. Hudson, R. J., Stuart, A. N., Huang, D. M. & Kee, T. W. What Next for Singlet Fission in Photovoltaics? The Fate of Triplet and Triplet-Pair Excitons. *J. Phys. Chem. C* **126**, 5369–5377 (2022).
3. Ramesh, S. *et al.* Tailoring the Energy Manifold of Quasi-Two-Dimensional Perovskites for Efficient Carrier Extraction. *Adv. Energy Mater.* **2103556**, 1–11 (2022).
4. Baikie, T. K. *et al.* Photosynthesis re-wired on the pico- second timescale.
5. Kasha, M. Characterization of electronic transitions in complex molecules. *Discuss. Faraday Soc.* **9**, 14–19 (1950).
6. González-Rodríguez, D. *et al.* Screening electronic communication through ortho-, meta- And para-substituted linkers separating subphthalocyanines and C60. *Chem. - A Eur. J.* **14**, 7670–7679 (2008).
7. Haines, P. *et al.* Screening Nanographene-Mediated Inter(Porphyrin) Communication to Optimize Inter(Porphyrin–Fullerene) Forces. *Adv. Energy Mater.* **11**, 2100158 (2021).
8. Zirzmeier, J. *et al.* Singlet fission in pentacene dimers. *Proc. Natl. Acad. Sci.* **112**, 5325–5330 (2015).
9. Richardson, D. E. & Taube, H. Electronic Interactions in Mixed-Valence Molecules as Mediated by Organic Bridging Groups. *J. Am. Chem. Soc.* **105**, 40–51 (1983).
10. Marvaud, V., Launay, J. P. & Joachim, C. Electron transfer through 2,7,9,10-tetraazaphenanthrene: a quantum ‘interference’ effect? *Chem. Phys.* **177**, 23–30 (1993).

11. Gust, D. *et al.* Triplet and Singlet Energy Transfer in Carotene-Porphyrin Dyads: Role of the Linkage Bonds. *J. Am. Chem. Soc.* **114**, 3590–3603 (1992).
12. Patoux, C., Coudret, C., Launay, J.-P., Joachim, C. & Gourdon, A. Topological Effects on Intramolecular Electron Transfer via Quantum Interference. *Inorg. Chem.* **36**, 5037–5049 (1997).
13. Cho, S. *et al.* Perturbation of electronic states and energy relaxation dynamics in a series of phenylene bridged ZnII porphyrin dimers. *J. Phys. Chem. C* **111**, 14881–14888 (2007).
14. Martin, M. M., Lungerich, D., Haines, P., Hampel, F. & Jux, N. Electronic Communication across Porphyrin Hexabenzocoronene Isomers. *Angew. Chemie Int. Ed.* **58**, 8932–8937 (2019).
15. Cotic, A. *et al.* A Photoinduced Mixed Valence Photoswitch. *Phys. Chem. Chem. Phys.* (2022) doi:10.1039/D2CP01791A.
16. Sampaio, R. N. *et al.* Kinetics teach that electronic coupling lowers the free-energy change that accompanies electron transfer. *Proc. Natl. Acad. Sci.* **115**, 7248–7253 (2018).
17. Hu, K. *et al.* Kinetic pathway for interfacial electron transfer from a semiconductor to a molecule. *Nat. Chem.* **8**, 853–859 (2016).
18. Bignozzi, C. A. *et al.* Oligomeric Dicyanobis(polypyridine)ruthenium(II) Complexes. Synthesis and Spectroscopic and Photophysical Properties. *Inorg. Chem.* **28**, 4350–4358 (1989).
19. Amadelli, R., Argazzi, R., Bignozzi, C. A. & Scandola, F. Design of Antenna-Sensitizer Polynuclear Complexes. Sensitization of Titanium Dioxide with [Ru(bpy)₂(CN)₂]₂Ru(bpy(COO)₂)₂²⁻. *J. Am. Chem. Soc.* **112**, 7099–7103 (1990).
20. Arias-Rotondo, D. M. & McCusker, J. K. The photophysics of photoredox catalysis: A

- roadmap for catalyst design. *Chem. Soc. Rev.* **45**, 5803–5820 (2016).
21. Cerfontaine, S. *et al.* Tuning the excited-state deactivation pathways of dinuclear ruthenium(II) 2,2'-bipyridine complexes through bridging ligand design. *Dalton Trans.* **49**, 8096–8106 (2020).
 22. Cerfontaine, S. *et al.* Efficient Convergent Energy Transfer in a Stereoisomerically Pure Heptanuclear Luminescent Terpyridine-Based Ru(II)-Os(II) Dendrimer. *Inorg. Chem.* **59**, 14536–14543 (2020).
 23. Cerfontaine, S., Wehlin, S. A. M., Elias, B. & Troian-Gautier, L. Photostable Polynuclear Ruthenium(II) Photosensitizers Competent for Dehalogenation Photoredox Catalysis at 590 nm. *J. Am. Chem. Soc.* **142**, 5549–5555 (2020).
 24. Damrauer, N. H. & McCusker, J. K. Ultrafast dynamics in the metal-to-ligand charge transfer excited-state evolution of [Ru(4,4'-diphenyl-2,2'-bipyridine)₃]²⁺. *J. Phys. Chem. A* **103**, 8440–8446 (1999).
 25. Liu, Y. *et al.* Ultrafast Ligand Exchange: Detection of a Pentacoordinate Ru(II) Intermediate and Product Formation. *J. Am. Chem. Soc.* **131**, 26–27 (2009).
 26. Rachford, A. A. & Rack, J. J. Picosecond Isomerization in Photochromic Ruthenium–Dimethyl Sulfoxide Complexes. *J. Am. Chem. Soc.* **128**, 14318–14324 (2006).
 27. McFarland, S. A., Lee, F. S., Cheng, K. A. W. Y., Cozens, F. L. & Schepp, N. P. Picosecond dynamics of nonthermalized excited states in tris(2,2-bipyridine)ruthenium(II) derivatives elucidated by high energy excitation. *J. Am. Chem. Soc.* **127**, 7065–7070 (2005).
 28. Ramakrishna, G. *et al.* Ultrafast dynamics and excited state deactivation of [Ru(bpy)

- 2Sq]⁺ and Its derivatives. *J. Phys. Chem. B* **110**, 10197–10203 (2006).
29. Bhasikuttan, A. C., Suzuki, M., Nakashima, S. & Okada, T. Ultrafast Fluorescence Detection in Tris (2 , 2 ' -bipyridine) ruthenium (II) Complex in Solution : Relaxation Dynamics Involving Higher Excited States. *J. Am. Chem. Soc.* **124**, 8398–8405 (2002).
30. Cerfontaine, S. *et al.* MLCT Excited-State Behavior of Trinuclear Ruthenium(II) 2,2'-Bipyridine Complexes. *Inorg. Chem.* **60**, 366–379 (2021).
31. Rutherford, T. J., Van Gijte, O., Kirsch-De Mesmaeker, A. & Keene, F. R. Stereoisomers of Mono-, Di-, and Triruthenium(II) Complexes Containing the Bridging Ligand 1,4,5,8,9,12-Hexaazatriphenylene and Studies of Their Photophysical Properties. *Inorg. Chem.* **36**, 4465–4474 (1997).
32. Campagna, S. Absorption spectra, photophysical properties, and redox behavior of stereochemically pure dendritic ruthenium(II) tetramers and related dinuclear and mononuclear complexes. *Inorg. Chem.* **38**, 692–701 (1999).
33. Browne, W. R., O'Connor, C. M., Villani, C. & Vos, J. G. Separation and photophysical properties of the $\Delta\Delta$, $\Lambda\Lambda$, $\Delta\Lambda$, and $\Lambda\Delta$ stereoisomers of a dinuclear ruthenium(II) complex. *Inorg. Chem.* **40**, 5461–5464 (2001).
34. Damrauer, N. H. *et al.* Femtosecond Dynamics of Excited-State Evolution in [Ru(bpy)₃]²⁺. *Science* **275**, 54–57 (1997).
35. Brown, A. M. *et al.* Vibrational Relaxation and Redistribution Dynamics in Ruthenium(II) Polypyridyl-Based Charge-Transfer Excited States: A Combined Ultrafast Electronic and Infrared Absorption Study. *J. Phys. Chem. A* **122**, 7941–7953 (2018).
36. Aydogan, A. *et al.* Accessing Photoredox Transformations with an Iron(III) Photosensitizer and Green Light. *J. Am. Chem. Soc.* (2021) doi:10.1021/jacs.1c06081.

37. Elgrishi, N., Chambers, M. B., Wang, X. & Fontecave, M. Molecular polypyridine-based metal complexes as catalysts for the reduction of CO₂. *Chem. Soc. Rev.* **46**, 761–796 (2017).

Supplementary Files

This is a list of supplementary files associated with this preprint. Click to download.

- [CoticetalSINatureChem.pdf](#)
- [flatCadranelepc.pdf](#)